Design and Analysis of a Permanent Magnet Spherical Actuator

Liang Yan, *Member, IEEE*, I-Ming Chen, *Senior Member, IEEE*, Chee Kian Lim, Guilin Yang, *Member, IEEE*, Wei Lin, *Member, IEEE*, and Kok-Meng Lee, *Fellow, IEEE/ASME*

***Abstract*—This paper has proposed a 3-DOF spherical actuator consisting of a ball-shaped rotor with a full circle of permanent-magnet (PM) poles and a spherical-shell-like stator with two layers of circumferential air-core coils. One key feature of this design is the parametrization of PM and coil poles. Based on the torque model of the PM spherical actuator, the relationship between poles' parameters and torque output can be demonstrated. As a result, the actuator design aiming at achieving maximum torque output can be carried out from the relationships. Another advantage of this spherical actuator is its singularity-free workspace, which is verified with the actuator torque model and condition numbers.**

***Index Terms*—Actuator design, spherical actuator, torque model.**

I. Introduction

THE RAPID advances in robotics and automatic manufacturing have brought about the demand of multi-degree-of-freedom (multi-DOF) actuators to replace the conventional bulky spherical motion mechanisms that are composed of several single-axis actuators. One effective option is the spherical actuator which can achieve 2 or 3-DOF rotational motions in only one joint. This type of actuator has the virtues of compactness, uniform motion, and nonsingularity, etc. Williams and Laithwaite *et al*. have done some pioneering work on the spherical induction motor [1]. This induction motor can achieve 2-DOF spherical motion. Its magnetic field and torque were analyzed by Davey *et al*. [2]. A 3-DOF induction spherical motor was conceptualized by Vachtsevanos *et al*. [3]. Owing to the complexity in mechanical and winding design, it is difficult to produce a prototype. Lee *et al*. [4], [5] have developed a variable-reluctance spherical motor (VRSM), which has a compact size as well as a desirable working range. A nonlinear torque model relates the current inputs to the torque output [6]. Permanent magnet (PM) spherical actuators, which can achieve either 2-DOF or 3-DOF motion, have been developed by Wang *et al*. [7], [8]. The rotor is entirely composed of magnetized rare earth materials and three or four coils are mounted on the stator. Chirikjian and Stein [9] have made a spherical stepper with a PM-pole rotor and a stator with an array of coils. Difference in the symmetric layout of the rotor and the stator poles allows stepping motion in three orientations. Yang and Baek [10] proposed a 3-DOF spherical actuator composed of a rotor with two magnet poles and a stator with five electromagnet poles. The rotor can make an arbitrary orientation and a spin. Kahlen *et al*. [11] developed a spherical motor consisting of a rotor with 112 PM poles and a stator with 96 windings. The poles were arranged symmetrically corresponding to longitude and latitude of a globe. The actuator torque was calculated numerically. Dehez *et al*. [12] developed a 2-DOF spherical induction motor composed of a two-layer rotor with teeth surrounded by five inductors. The rotor can achieve unlimited angular range.

In this research, a 3-DOF PM spherical actuator is proposed [13], [14]. This spherical actuator features the flexible structure, i.e., the structure of two major torque generating elements, PM and coil poles, are parameterized, which is useful for observing the relationship between structure parameters and torque output. This provides a way to increase the actuator torque output by selecting structure dimensions. Furthermore, more PM and coil poles could be incorporated to increase the working range as well as the motion resolution of this spherical actuator. In the following sections, the actuator torque model is derived based on the poles' parameters [15]. Then values of these parameters are determined based on the torque model to achieve maximum torque output. Additionally, the singularity-free workspace of this spherical actuator is verified.

Manuscript received May 11, 2007; revised November 1, 2007. Recommended by Technical Editor M. E. Benbouzid. This work was supported by a collaborative research project under Grant U02-A-O40B for Nanyang Technological University, Singapore Institute of Manufacturing Technology, and Georgia Institute of Technology.

L. Yan and C.-K. Lim are with the School of Mechanical and Aerospace Engineering, Nanyang Technological University, Singapore 639798, Singapore (e-mail: yanliang@pmail.ntu.edu.sg; cklim@ntu.edu.sg).

I-M. Chen is with the School of Mechanical and Aerospace Engineering, Nanyang Technological University, Singapore 639798, Singapore.

G. Yang and W. Lin are with Mechatronics Group, Singapore Institute of Manufacturing Technology, 71 Nanyang Drive, Singapore 638075, Singapore (e-mail: glyang@simtech.a-star.edu.sg; wlin@SIMTech.a-star.edu.sg).

K.-M. Lee is with George W. Woodruff School of Mechanical Engineering, Georgia Institute of Technology, Atlanta, Georgia 30332 USA (e-mail: kok-meng.lee@me.gatech.edu).

Color versions of one or more of the figures in this paper are available online at http://ieeexplore.ieee.org.

Digital Object Identifier 10.1109/TMECH.2008.918573

II. Poles Geometry and Torque Model

A. Working Principle

The working principle of this spherical actuator is illustrated in Fig. 1. This spherical actuator consists of a ball-shaped rotor with a full circle of PM poles and a spherical-shell-like stator with two layers of circumferential air-core coils. The rare earth PMs can generate high flux density within the actuator, and the air-core coils may simplify the torque model in a linear fashion. With pairs of coils activated in two longitudinal directions, the rotor creates tilting motions in two orthogonal directions as shown in Fig. 1(a) and (b). By energizing the rest of the circumferential coils, the rotor can spin about its axis. Therefore, through varying the current input of coils, the actuator

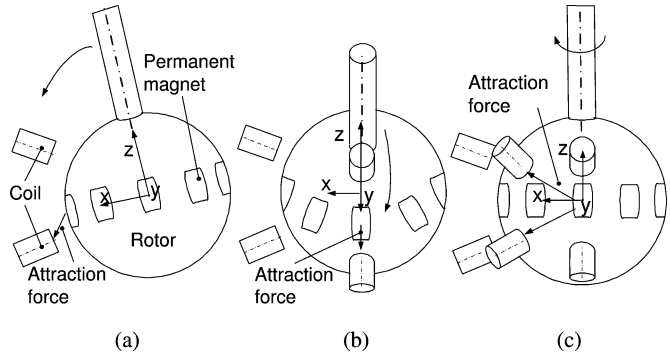

Fig. 1. 3-DOF motion of spherical actuator. (a) First tilting motion. (b) Second tilting motion. (c) Spinning motion.

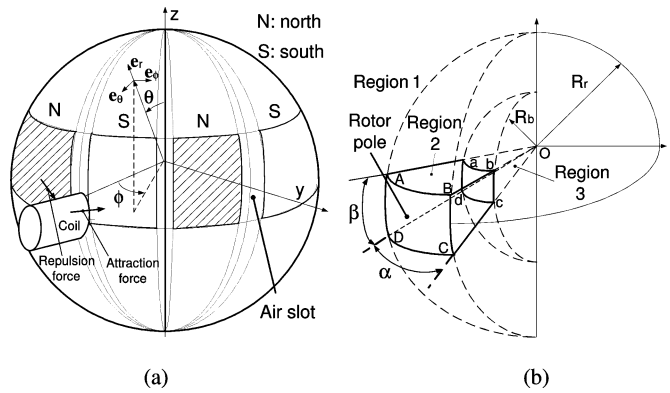

Fig. 2. Arrangement and configuration of rotor poles. (a) Rotor poles along equator. (b) Single rotor pole.

can produce any desirable 3-DOF rotational motion within the workspace.

B. Geometric Parameters of Poles

In order to facilitate the actuator design, geometric parameters of PM and coil poles of the spherical actuator are presented as follows.

1) PM-Pole Parameters: The PM rotor poles in alternate magnetization directions are placed around the rotor equator as shown in Fig. 2(a). There are air slots in between PM poles. And the regions on top and bottom of the rotor can also be air or low-density materials such as aluminum. These air slots generalize the study of poles arrangement. Moreover, because the density of aluminum (2.7 g/cm^3) or air (1.29×10^{-3} g/cm^3) is much lower than that of rare earth material (NdFeB 7.8 g/cm^3), the inertia moment of the rotor can be reduced considerably (about 50%). This alternately magnetized poles configuration leads to the periodical variation of the magnetic field distribution circumventing the rotor. As indicated in the figure, a coil can produce an attraction force and a repulsion force by interacting with two neighboring PM poles. Thus, this poles configuration may generate higher torque compared with the configuration with same polarization.

Fig. 2(b) presents the shape of a single rotor pole—an approximated dihedral cone enclosed by $ABCD$ and $abcd$. The dihedral cone can be specified by four parameters: longitudinal angle α, latitudinal angle β, rotor radius R_r, and rotor core radius R_b. Modeling a single pole as a dihedral cone has several benefits. First, due to the 3-DOF rotational motion of the rotor, the spherical surface of the dihedral-cone-shaped pole can avoid the interference between coils and PM poles, while making full use of the rotor workspace. Second, the volume of the rotor pole can now be specified in spherical coordinates, which facilitates the formulation of the actuator torque. Third, by varying the parameters of the dihedral cone, the study of optimum magnet-pole pattern can be carried out.

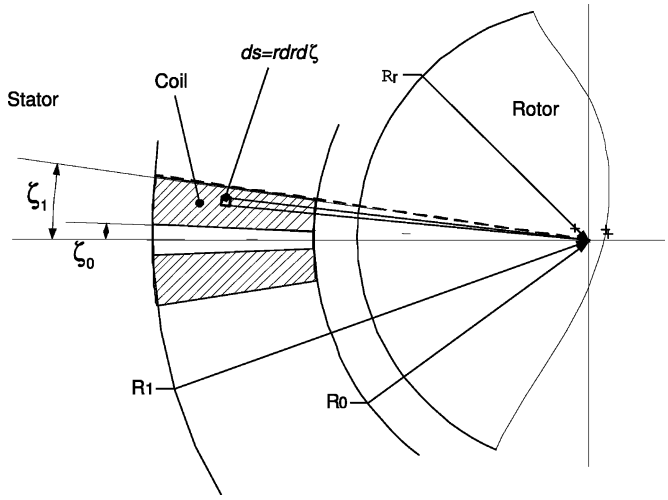

Fig. 3. Sectional view of the coil shape.

2) Coil Parameters: A conical-shaped coil is utilized in this PM spherical actuator as shown in Fig. 3. The sectional area of the coil can be specified by four parameters, i.e., R_0 the distance from the rotor center to the top surface of the coil, R_1 the distance from the rotor center to the bottom surface of the coil, ζ_0 the inner surface angle of the coil, and ζ_1 the outer surface angle of the coil. This geometric shape can take advantage of the space surrounding the rotor effectively. It can also facilitate the actuator torque formulation in the spherical coordinates. In addition, for actual products, cylindrical-shaped coil could be utilized. When considering the wiring on the coil, this coil can be approximated with a conical-shaped coil. Thus, the torque model can still be employed with certain modifications.

C. Torque Model

By using the parameters of PM and coil poles, the torque model for the spherical actuator has been derived, as indicated in Table I [14]. In these equations, $\mathbf{J} = [J_1, J_2, \ldots, J_N]$ is the current density passing through ith coil ($i = 1, 2, \ldots, N$); μ_0 is the permeability of free space having value of $4\pi \times 10^{-7}$ H/m; M_0 is the magnitude of the residual magnetization vector (A/m); μ_m is the dimensionless relative recoil permeability of PM having typical value between 1.05 and 1.2; μ_r is the relative permeability of ferromagnetic material such as soft iron having value larger than 4000.

The torque matrix $\boldsymbol{Q}$ is completely determined by positions of coil axis (θ_i, ϕ_i) in spherical coordinates, which, in turn,

TABLE I
EQUATIONS USED FOR PROTOTYPE DESIGN

Torque model	$\mathbf{T}=Tc\,\boldsymbol{Q}\,\mathbf{J}$	Eqn. (1)
Torque matrix	$\boldsymbol{Q}=\begin{bmatrix} g_x(\theta_1,\phi_1)\, g_x(\theta_2,\phi_2)\cdots g_x(\theta_N,\phi_N) \\ g_y(\theta_1,\phi_1)\, g_y(\theta_2,\phi_2)\cdots g_y(\theta_N,\phi_N) \\ g_z(\theta_1,\phi_1)\, g_z(\theta_2,\phi_2)\cdots g_z(\theta_N,\phi_N) \end{bmatrix}$	Eqn. (2)
Constant Tc	$T_c=\frac{15}{16}\sqrt{\frac{35}{2}}\mu_0 M_0 a c d_4 R_c G_\zeta$	Eqn. (3)
Constants a, b, c	$a \pm bi \equiv \int_0^{2\pi} f(\phi)e^{-im\phi}d\phi,\ (m=\pm 4)$	Eqn. (4)
	$c/\sqrt{\pi} \equiv \int_0^{\pi}\sqrt{\frac{2n+1}{4\pi}\frac{(n-m)!}{(n+m)!}}\sin^2\theta[P_n^m(\cos\theta)]d\theta$ $(n=4, m=\pm 4)$	Eqn. (5)
	$f(\phi)=(-1)^{p-1}\cos[\phi-\frac{\pi}{4}(p-1)],\ p=1,2,...,8.$	Eqn. (6)
	$\frac{\pi}{4}(p-1)-\frac{\alpha}{2}<\phi<\frac{\pi}{4}(p-1)+\frac{\alpha}{2}$	Eqn. (7)
	$\frac{\pi}{2}-\frac{\beta}{2}<\theta<\frac{\pi}{2}+\frac{\beta}{2}$	Eqn. (8)
Constant d_4	$d_4=-d_4^{\top}/d_4^{\perp}$	Eqn. (9)
	$d_4^{\top}=R_r^6+\frac{9\mu_m R_b^6 R_r^9}{4(\mu_r-\mu_m)R_b^9-(4\mu_r+5\mu_m)R_r^9}$	
	$d_4^{\perp}=5(\mu_m-1)+\frac{9\mu_m(4\mu_r+5\mu_m)R_r^9}{4(\mu_r-\mu_m)R_b^9-(4\mu_r+5\mu_m)R_r^9}$	
Constant R_c	$R_c=R_0^{-2}-R_1^{-2}$	Eqn. (10)
Constant G_ζ	$G_\zeta=G_\zeta''-\frac{3G_\zeta'}{4}$	Eqn. (11)
	$G_\zeta'=\frac{1}{5}\sin^5\zeta_1-\frac{1}{5}\sin^5\zeta_0$	
	$G_\zeta''=\frac{1}{5}\cos^4\zeta_0\sin\zeta_0-\frac{1}{15}\cos^2\zeta_0\sin\zeta_0-\frac{2}{15}\sin\zeta_0-\frac{1}{5}\cos^4\zeta_1\sin\zeta_1+\frac{1}{15}\cos^2\zeta_1\sin\zeta_1+\frac{2}{15}\sin\zeta_1$	
Magnetic field	$B_{Ir}=\frac{15\mu_0 M_0 a c d_4}{8\pi}\sqrt{\frac{35}{2}}r^{-6}\sin^4\theta\cos 4\phi$	Eqn. (12)

is determined by rotor orientations with respect to the stator frame. The torque constant T_c is calculated with coefficients a, c, d_4, R_c, and G_ζ. These coefficients are defined by structural parameters of PM poles (α, β, R_b, and R_r) and those of coils (R_0, R_1, ζ_0, and ζ_1).

According to equations in Table I, it can be found that the coefficients a, c, d_4, R_c, and G_ζ are affected by different pole parameters separately. Therefore, appropriate pole parameters can be selected to achieve the maximum value for each coefficient, thus to maximize the torque output.

III. DESIGN OF PM POLES

As indicated in (3), high values of coefficients a, c, and d_4 contribute to high torque output of the spherical actuator. Therefore, the major purpose of PM pole design is to select appropriate values of α, β, R_r, and R_b to achieve high values of these coefficients, and thus, high torque output.

A. Longitudinal Angle α Versus a

Constant a can be calculated from α through (4) and (7). Because eight PM poles are installed along the equator of the rotor, the maximum value of α is $45°$. The relation between α and a is shown in Fig. 4(a). According to the figure, a increases with the increase of α. Therefore, theoretically the optimum value of α is $45°$. From a physical perspective, large α represents large volume of magnetized material, which can create large flux density, thus, large torque output generally.

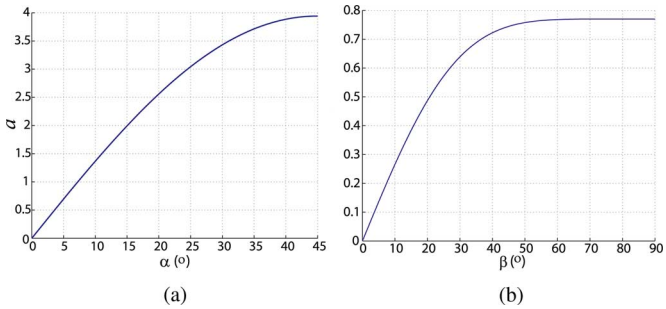

(a) (b)

Fig. 4. Determination of angular parameters of PM pole. (a) Parameter α versus constant a (b) Parameter β_1 versus constant c.

B. Latitudinal Angle β Versus c

Similarly, constant c is calculated from (5) and the integral range in (8) specified by the angle β (0–180°). Let $\beta_1=\beta/2$, where β_1 varies from 0 to 90°. The relation between β_1 and the constant c is shown in Fig. 4(b). It shows that after $\beta_1=60°$, c reaches the largest value. Hence, high torque output can be achieved within the range of $60° \le \beta_1 \le 90°$. For $\beta_1 > 60°$, the inertia moment of the rotor increases, which affects the dynamic performance of the spherical actuator. Thus, the optimum value of β_1 should be 60°. The curve in Fig. 4(b) has the following physical meaning. The increase of β_1 indicates increase of magnet volume, which leads to high flux density, and thus, high torque output. However, when β_1 increases to a certain degree, the volume increase of the magnet is much less. Furthermore, when β is large, the distance between neighboring PM poles becomes smaller, thus the reducing effect of flux density between these two opposite magnetized poles becomes evident. Therefore, the effect of β on the increase of actuator torque output is negligible when it is large.

C. Rotor Radius R_r Versus d_4

To simplify the study of R_r, let $R_b=0$. Fig. 5(a) illustrates the relationship between R_r and d_4. Approximately, d_4 increases exponentially with respect to R_r. This is due to the fact that the increase of magnet volume with respect to R_r is fast when R_r is large, which yields fast increase of magnetic field and torque output. Therefore, a large rotor is preferred to create high flux density as well as high torque output. Due to mechanical constraint in this actuator, the rotor size is chosen as 46.5 mm for prototype development.

D. Rotor Core Radius R_b Versus d_4

Similarly, from the torque model, large d_4 is preferred for high torque. With $R_r=46.5$ mm, the relation between R_b and d_4 is shown in Fig. 5(b). It can be seen that small R_b produces

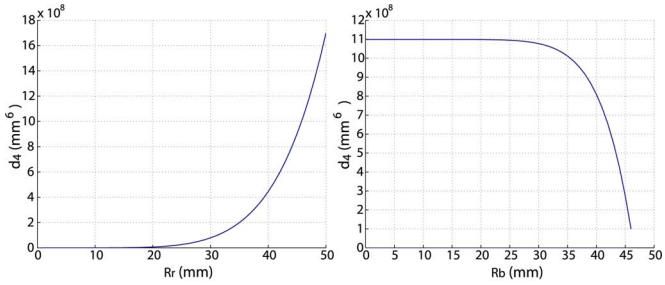

(a) (b)

Fig. 5. Determination of radial parameters of PM pole. (a) Parameter R_r versus d_4. (b) Parameter R_b versus d_4.

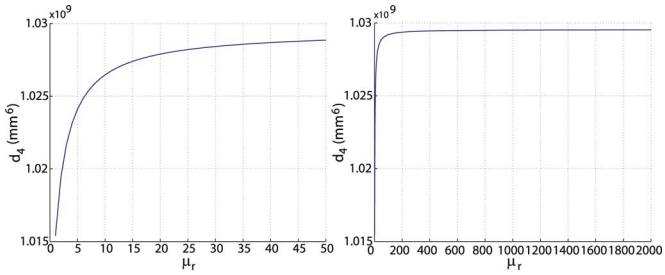

(a) (b)

Fig. 6. Effect of μ_r on d_4. (a) $0 < \mu_r < 50$. (b) $0 < \mu_r < 2000$.

large d_4, and thus, high torque output as well as high flux density. However, when R_b is reduced to a certain size, i.e., 23 mm, there is no increase of constant d_4. In other words, when $R_b < 23$, the decrease of R_b does not contribute much to increase magnetic flux density and torque output. This justifies the assumption of $R_b = 0$ when evaluating the effect of R_r. The relation in Fig. 5(b) can be explained as follows. It is known that the larger is R_b, the smaller the rotor volume is. When R_b is near to the rotor radius, the rotor is very thin. The flux density and actuator torque drop down very fast. However, when R_b is less than a certain degree, the volume increase of magnetized material is much less and its contribution to the flux density and torque output is negligible. As a result, the optimum R_b is equal to 23 mm. This design creates a hollow space at the rotor center for assembly of a spherical bearing.

E. Relative Permeability μ_r Versus d_4

Constant d_4 in (9) can also be used to observe the effect of relative permeability μ_r of ferromagnetic materials (rotor core) on the torque output of the spherical actuator. According to (9), the relation between μ_r and d_4 can be seen in Fig. 6. When μ_r is less than 50 [Fig. 6(a)], its effect on d_4 is evident. However, when μ_r is greater than 400 [Fig. 6(b)], d_4 does not change with respect to μ_r. In other words, when the permeability of the rotor core is very large, the impact of material selection of the rotor core on the torque output of the PM spherical actuator becomes invariable.

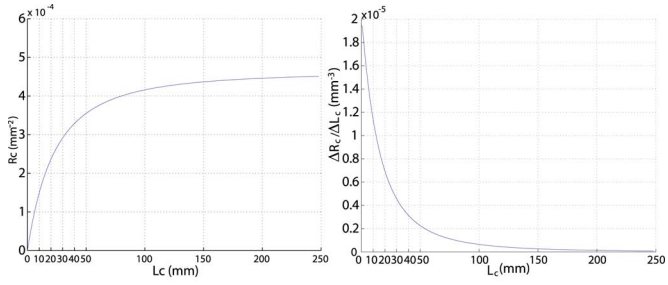

(a) (b)

Fig. 7. Effect of L_c on R_c. (a) R_c versus L_c. (b) Increasing speed of R_c versus L_c.

F. Result of PM Pole Design

The dimensions of the PM pole (NdFeB) have been determined based on the aforesaid discussion, i.e., $\alpha = 45^\circ$, $\beta = 120^\circ$, $R_r = 46.5$ mm and $R_b = 23$ mm. However, for the actual prototype, $\alpha = 40^\circ$ is used to replace $\alpha = 45^\circ$ and $\beta = 70^\circ$ is used to replace $\beta = 120^\circ$ to facilitate the fabrication. It can be seen from Fig. 4 that this replacement does not change the torque output much. Instead, the size reduction of PM poles provides a space for fixture design to hold PM poles.

IV. Coil Design

Besides the PM pole, the other critical element generating actuator torque is the air-core coil. Similar to the PM pole design, the effect of coil parameters on the torque output of the actuator can be presented so that values of coil parameters can be chosen to maximize the torque capacity. In addition to the geometric parameters of coils, large number of winding turns also benefit high torque output. Several factors of fabricating coils that can increase the winding turns are discussed here, such as the packing patterns of coils, and diameter of wires.

A. Geometric Parameters of the Coil

As shown in Fig. 3, four parameters are used to specify the coil shape, i.e., R_0, R_1, ζ_0, and ζ_1. R_0, and R_1 can be replaced by the length of coil denoted as $L_c = R_1 - R_0$. In the following discussion, the values of three parameters ζ_0, ζ_1, and L_c will be determined.

1) Determination of Coil Length: Constant R_c is defined with R_0 and R_1 (10). Let $R_0 \approx R_r$(46.5 mm), i.e., the coil tip is very close to the rotor surface, as the flux density is high near the rotor surface. By using L_c, (10) becomes

$$R_c = R_0^{-2} - R_1^{-2} = R_r^{-2} - (R_r + L_c)^{-2}. \qquad (13)$$

The relation between L_c and R_c is illustrated in Fig. 7(a). It can be seen that increasing L_c, R_c will increase, and thus, torque output increases. Large L_c implies that more wires are enclosed in the winding volume, for high actuator torque output. The rate of increment in R_c versus L_c is illustrated in Fig. 7(b). It can be found that when the length of coil exceeds 230 mm, $\Delta R_c/\Delta L_c$ is close to 0. R_c does not increase further when $L_c > 230$ mm as the magnetic flux density becomes very small at the distance far away from the rotor surface. The increased wire winding in this

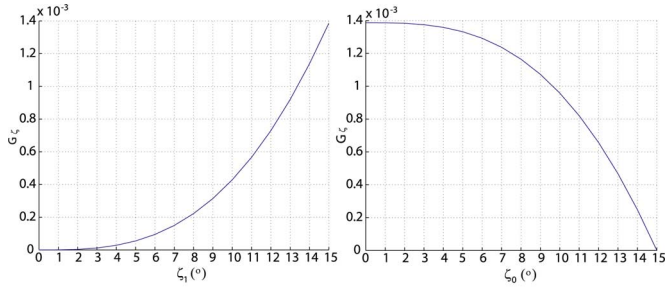

(a) (b)

Fig. 8. Determination of angular parameters of coil. (a) ζ_1 versus G_ζ ($\zeta_0 = 0$). (b) ζ_0 versus G_ζ ($\zeta_1 = 15^\circ$).

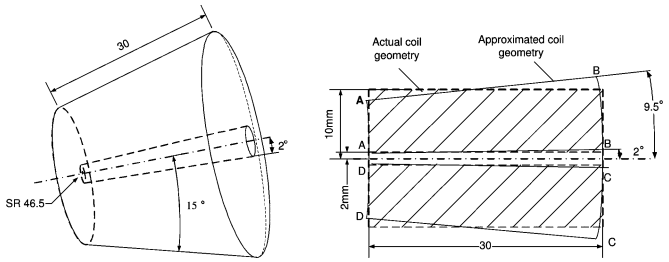

(a) (b)

Fig. 9. Geometry of coil poles. (a) Optimized conical coil. (b) Actual coil (section view).

region therefore has negligible effect on the torque generation. Hence, to achieve a high torque output, L_c can be kept at 230 mm. Nevertheless, according to $\Delta R_c/\Delta L_c$ curve in Fig. 7(b), the increment rate $\Delta R_c/\Delta L_c$ for $L_c = 30$ mm is only one-quarter of the maximum $\Delta R_c/\Delta L_c$, i.e., the torque contribution from coil turns beyond $L_c = 30$ mm is not evident. Excessive winding increases the electrical power consumption. Therefore, $L_c = 30$ mm can be chosen for the actual coil design.

2) Determination of Coil Angles:

Determination of ζ_1

To facilitate the discussion, let $\zeta_0 = 0$. According to (11), the relation between ζ_1 and G_ζ is plotted in Fig. 8(a). It can be found that the effect of ζ_1 on G_ζ is prominent. With reference to Fig. 3, when ζ_1 is large, the same increment of ζ_1 results in a large increment of wire length, and thus, the torque increases fast. The maximum value of ζ_1 is approximately 15° because there are 12 coils for each layer of stator poles. To achieve high torque output, $\zeta_1 = 15^\circ$ is the optimum value.

Determination of ζ_0

The coil core angle ζ_0 also affects the actuator torque output capacity. By fixing ζ_1 at 15°, the relation between G_ζ and ζ_0 is plotted in Fig. 8(b). When ζ_0 increases, the value of G_ζ decreases, thus the torque output decreases. However, when ζ_0 is less than 2°, G_ζ is approximately a constant of 1.39×10^{-3}. Usually the smaller ζ_0, the longer the winding length and the larger the torque output. But when ζ_0 is smaller than a certain value, variation of ζ_0 does not affect the wire length on the coil evidently and the variation of torque is ignorable. This justifies the condition of $\zeta_0 = 0$ when we discuss the value of ζ_1. The value of $\zeta_0 = 2^\circ$ offers two additional advantages. First, it reduces the electrical power consumption whereas the torque output is not affected. Second, it provides the space for the design of coil frame on which the wire is wound. Therefore, $\zeta_0 = 2^\circ$ can be used as the optimum value for the coil design.

3) Optimized and Actual Coil Structures: Thus far, a coil geometry has been obtained as illustrated in Fig. 9(a). However, in the actual prototype, off-the-shelf cylindrical coils [Fig. 9(b)] are utilized to simplify the fabrication. It has an inner radius (R_{ci}) of 2 mm, outer radius (R_{co}) of 10 mm and a length (L_c) of 30 mm. It could be approximated with a conical coil with $\zeta_0 = 2^\circ$, $\zeta_1 = 9.5^\circ$, and $L_c = 30$ mm in terms of the winding volume. It can be seen from Fig. 8(a) that the value of G_ζ (1.39×10^{-3}) at $\zeta_1 = 15^\circ$ is approximately four times the value (3.5×10^{-4}) at $\zeta_1 = 9.5^\circ$.

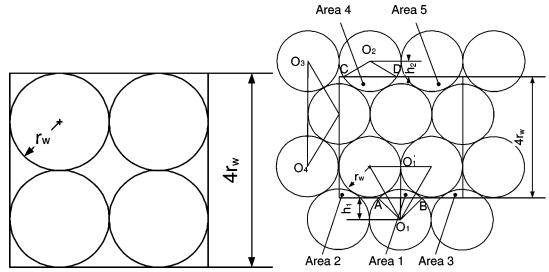

(a) (b)

Fig. 10. Wire packing patterns. (a) Regular pattern. (b) Staggering pattern.

B. Increase Number of Winding Turns

Current density of the coil is defined as the electric current passing through unit sectional area of the coil, i.e.,

$$J = \frac{\Delta I}{\Delta A} = \frac{\Delta N I_w}{\Delta A} \tag{14}$$

where I_w is the current passing through a single wire, and $\Delta I = \Delta N I_w$ is the total current passing through a cross-section ΔA of the coil. Therefore, increasing the number of winding turns within per unit sectional area of the coil improves the current density of the coil, and thus, the torque output capacity of the spherical actuator. Several approaches are discussed here to increase the number of winding turns.

1) Comparison of Packing Patterns: The packing pattern of winding affects the number of wire turns placed within a given area. Fig. 10(a) illustrates the regular packing pattern and Fig. 10(b) is the staggering pattern. The density of the patterns can be computed and compared for their effectiveness. Here, the stacking density is defined as the ratio of the occupied cross-sectional area of the wires and that of the designated square space (Fig. 10). For the regular pattern, the stacking density is

$$E_1 = \frac{4\pi r_w^2}{16 r_w^2} = 78.5\% \tag{15}$$

where r_w is the radius of the wire. As for the staggering packing pattern, the total area of wire sections within the square in

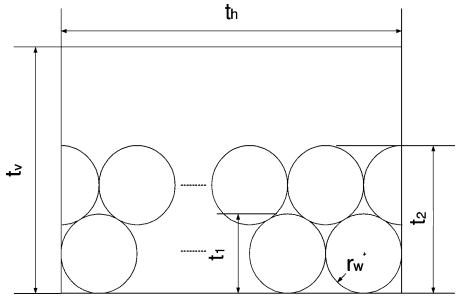

Fig. 11. Number of winding turns versus wire diameter.

Fig. 10(b) can be expressed as

$$A_t = 4\pi r_w^2 + 2\left[r_w^2 \arccos\left(\frac{h_1}{r_w}\right) - \sqrt{r_w^2 - h_1^2}h_1\right] + 2\left[r_w^2 \arccos\left(\frac{h_2}{r_w}\right) - \sqrt{r_w^2 - h_2^2}h_2\right]. \quad (16)$$

Hence, the stacking density is $E_2 = 87.2\%$. It shows that the staggering packing pattern offers 10% more stacking density than the regular packing pattern.

2) Reduction of Wire Diameter: Wire diameter affects the number of winding turns. Generally, small diameter of wires allows more turns of winding to occupy the same area. Analysis is carried out to estimate the increased coil turns due to diameter reduction of wires. Based on Fig. 11, the number of turns that occupies the sectional area can be computed as

$$N_{\text{turn}} = Int\left[1 + \frac{2}{\sqrt{3}}\left(\frac{t_v}{2r_w} - 1\right)\right] Int\left(\frac{t_h}{2r_w}\right) \quad (17)$$

where Int represents the integer of the result value. Suppose that there are two type of wires with radius of r_{w1} and r_{w2}. It can be found that $(t_v/2r_{w1}, t_v/2r_{w2} \gg 1)$

$$\frac{N_{\text{turn1}}}{N_{\text{turn2}}} \simeq \left(\frac{r_{w2}}{r_{w1}}\right)^2. \quad (18)$$

Given two examples, i.e., American wire gauge (AWG) 21 with $r_{w2} = 0.38$ mm and AWG24 with $r_{w1} = 0.225$ mm, it can be known that the ratio of winding turns $N_{\text{turn1}}/N_{\text{turn2}}$ is nearly equal to 3. Hence, the number of winding turns with AWG24 can increase about threefolds than the AWG21 wire.

3) Operating Temperature of Wires: Another important factor that affects the choice of the wire type is the operating temperature of insulation layer of wires. The electric wire used for winding includes the bare wire and the insulation layer. For each kind of insulation layer, there is a maximal working temperature, i.e., heat resistance grade. The highest heat resistance grade (Grade H) of wire, can withstand 220 °C. While the coil with thin wire is preferred for generating high torque, it also produces more heat due to the increased wire turns. Experiments are carried out on the working temperature of AWG21 and AWG24 wires. By using the AWG21 wire, the coil can work continuously with an input current of 3 A. However, the torque produced is small because of the less number of turns. Using AWG24 wire will have more turns and produce more heat. By using a simple cooling system, AWG24 wire can work stably in the spherical actuator.

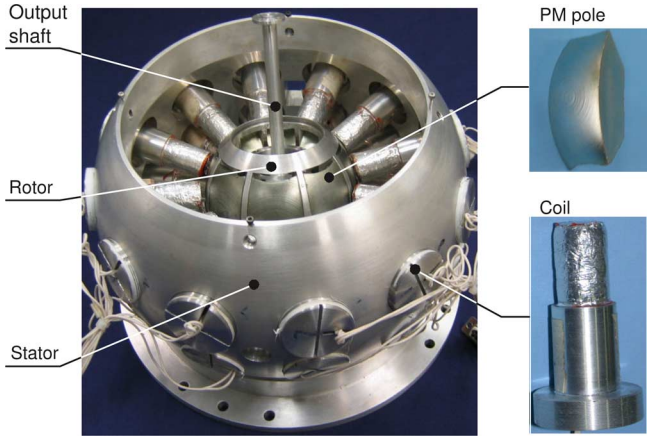

Fig. 12. Prototype of a spherical actuator.

TABLE II
STRUCTURE SPECIFICATIONS OF SPHERICAL ACTUATOR

Inner / outer stator radius	95 / 112.5 (mm)
Rotor radius	46.5 (mm)
Number of rotor poles (PM)	8
Number of stator poles (coil)	24 / 2 layers
Number of coil turns	1020
AWG	24
Maximum tilting angle	$\pm 11°$
Maximal spinning torque	4 (Nm)

C. Material of the Coil Frame

The material of the coil frame is important as it might generate eddy current under the action of the PM-pole rotor. If the size of the coil frame, especially the inner core angle ζ_0, is large, nonmetal material such as Delrin or laminated metal material is favorable for the coil frame because there is no or little eddy current produced. However, if angle ζ_0 is very small, the eddy current produced in the coil frame can be neglected. In this case, a metal material such as aluminium can be chosen as the coil frame material.

V. PROTOTYPE DEVELOPMENT

Based on the aforesaid analysis, a research prototype of the actuator has been developed (Fig. 12). The specification is listed in Table II. Eight PM poles are mounted along the rotor equator. Twenty-four circumferential holes are drilled through the stator shell and arranged in two layers symmetrically about the stator equator. Coils are mounted through these holes and point to the stator center. The threads in the holes allow coil frames to be screwed in and out for adjusting the coils' position. This configuration allows more coils to be incorporated so that the maximum tilting angle can be increased up to $\pm 45°$ and the resolution can also be improved.

The stator is made of aluminum due to its low cost and ease of fabrication. The inner radius of the stator (95 mm) is much

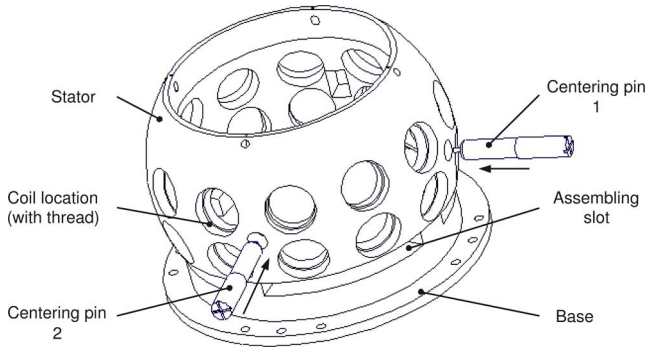

Fig. 13. Concentricity of the stator and rotor.

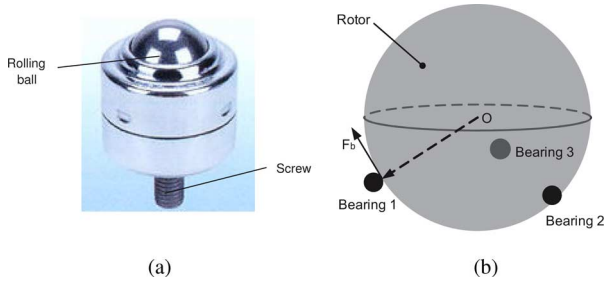

Fig. 14. Support spherical rotor with transfer bearings. (a) Transfer bearing [20]. (b) Rotor support.

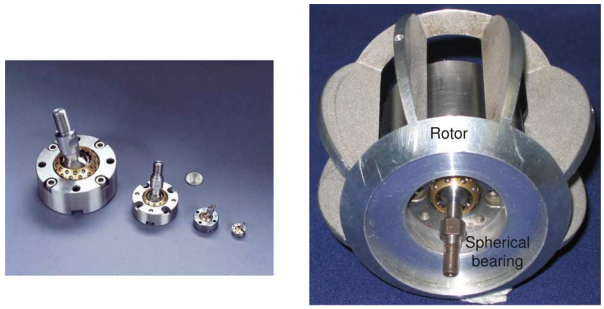

Fig. 15. Implementation of spherical bearing on the rotor. (a) Spherical bearing [16]. (b) Spherical bearing at the rotor center.

larger than that of the rotor (46.5 mm), so that the eddy current induced on the aluminum stator due to PM poles can be reduced significantly. Furthermore, large space between the rotor and the stator facilitates the flux density measurement inside the actuator and heat dissipation. For industrial products, the stator can be made from nonmetal material such as Delrin or laminated metal materials so that stator size can be reduced about 50%. Laminated ferromagnetic material not only reduces the eddy current significantly, but also improves the efficiency of the spherical actuator by "converging" the magnetic flux and reducing the magnetic energy loss.

A. Concentricity of the Stator and Rotor

In the assembly of the spherical actuator, it is required that the rotor is concentric with the stator. Two cylindrical holes separated 90° apart are drilled at the stator equator plane, as shown in Fig. 13. Likewise, two holes that are separated 90° apart and pointed to the rotor center are drilled at the rotor equator plane. Two centering pins can be inserted through the holes on the stator shell to the holes on the rotor. In this way, the concentricity of the rotor and the stator can be maintained.

B. Spherical Bearing

To secure the rotor position in the spherical actuator, a supporting mechanism is necessary. In the spherical actuator developed by Wang *et al.* [17], the spherical rotor is housed within the stator directly. Although a low friction coating was made on the stator inner surface, the sliding friction between the rotor and the stator might cause unfavorable effect on the rotor motion. In some spherical motors [5], [9], transfer bearings or analog are used to support the rotor. A typical transfer bearing is shown in Fig. 14(a). This bearing consists of a rolling ball on the top, which can create a rolling motion with respect to the contact surface. The screw on the other end can fix the bearing on the stator for adjusting its position. As indicated in Fig. 14(b), to support a spherical rotor stably, at least three transfer bearings are necessary. The rolling motion of these transfer bearings produces rolling frictions lower than the sliding frictions. Nevertheless, the friction torque from the transfer bearing relative to the rotor center is large due to the rotor radius. The nonnegligible resultant friction torque generated by transfer bearings may suppress the system efficiency. The effect of friction torque on the rotor of the VRSM has been analyzed by Zhou [6]. To effectively reduce the friction, an air-bearing system has been proposed by Lee *et al.* [18], [19]. Because the rotor floats on air, the friction is played down significantly. However, the requirement of air source complicates the application of this bearing system.

In our spherical actuator, a spherical bearing [Fig. 15(a)] [16] is employed to support the rotor housed in the stator. This spherical bearing can achieve a smooth 3-DOF rotational motion. The tilting motion range of this bearing is up to $\pm 35^\circ$. It can be assembled at the rotor center, as shown in Fig. 15(b). Because the friction produced by this spherical bearing is very small and the moment arm of the friction force is less than 4 mm, the friction torque produced by the spherical bearing is negligible. Compared with the air bearing, the implementation of this spherical bearing is also easy.

VI. Singularity-Free Workspace

Singularities here are defined as orientations of the rotor where no torque can be generated with respect to the rotor center even though large currents are supplied. These singularities have to be strictly avoided in the design because they may cause severe malfunctions.

In mathematical sense, the nonsingular orientations of the spherical actuator are the orientations that there exists at least one set of coil currents $[J_1, J_2, \ldots, J_N]^T$ to produce the desired actuator torque $\mathbf{T}$. This implies that the matrix $\boldsymbol{Q}$ must be a full-rank matrix for any rotor orientation within the workspace. A simple way to verify the nonsingularity of the spherical

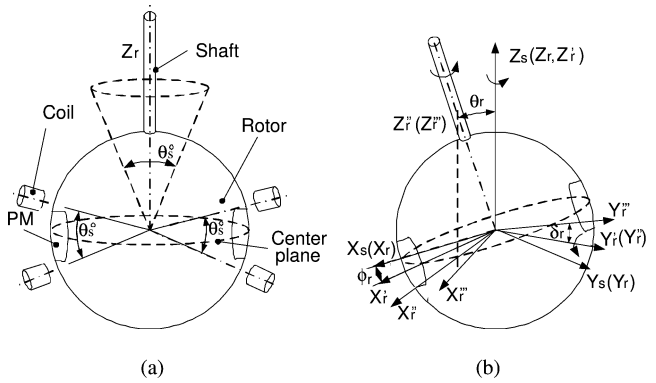

Fig. 16. Representation of the rotor orientation. (a) Working range of the rotor. (b) Rotation of the rotor frame.

actuator is to compute the rank of torque matrix $\boldsymbol{Q}$ for every attainable rotor orientation within the workspace. However, this method does not reveal how close the system is to singularity points. Therefore, a method based on condition number of $\boldsymbol{Q}$ is proposed. For nonsquare matrices, condition number is defined as

$$\text{cond}(\boldsymbol{Q}) = \left| \frac{\text{largest singular value}}{\text{smallest singular value}} \right|. \tag{19}$$

Ideally, when $\text{cond}(\boldsymbol{Q}) = 1$, the system being evaluated is in good condition. However, when $\text{cond}(\boldsymbol{Q}) \gg 1$, the system is ill-conditioned or nearly singular.

A. Representation of the Rotor Orientation

The workspace of the PM spherical actuator is shown in Fig. 16(a). A series of PM poles are mounted along the rotor equator, whereas the air-core coils are symmetrically mounted on the stator with respect to the stator equatorial plane, with two layers separated by an angular distance of θ_s. The rotor shaft can spin about its own z-axis, Z_r, in 360° without constraint. It can also incline to an extreme position that the axes of a PM pole and the coil are aligned. Thus, the z-axis of the rotor can move within a conical workspace with a conical angle of θ_s as shown in Fig. 16(a).

The orientation of the rotor frame with respect to the stator frame can be expressed by using Euler angles. Let the rotor frame be (X_r, Y_r, Z_r) and the stator frame be (X_s, Y_s, Z_s). In order to arrive at an arbitrary final orientation within the workspace, three rotor rotations have to take place in sequence [Fig. 16(b)]. The Euler ZYZ angle expression of the rotor orientation can be written as the multiplication of three body rotation matrices $\boldsymbol{R}_z(\phi_r)$, $\boldsymbol{R}_y(\theta_r)$, and $\boldsymbol{R}_z(\delta_r)$ [21]

$$\begin{bmatrix} X_s \\ Y_s \\ Z_s \end{bmatrix} = \boldsymbol{R} \begin{bmatrix} X_r \\ Y_r \\ Z_r \end{bmatrix} \tag{20}$$

where

$$\boldsymbol{R} = \boldsymbol{R}_z(\phi_r)\boldsymbol{R}_y(\theta_r)\boldsymbol{R}_z(\delta_r).$$

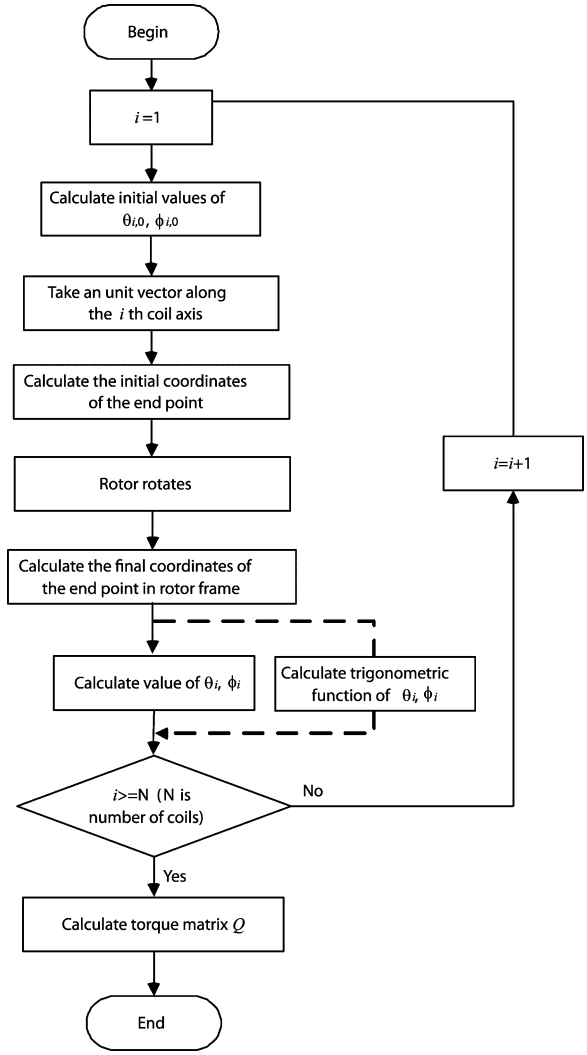

Fig. 17. Calculation of torque matrix from rotor orientation.

B. Computation of Torque Matrix $\boldsymbol{Q}$ From Rotor Orientation

The computing process of torque matrix $\boldsymbol{Q}$ from the rotor orientation is carried out as follows (Fig. 17).

Step 1: Computation of initial values of θ_i and ϕ_i. Because the positions of coil axes with respect to the rotor frame at the initial rotor orientation are known, it is easy to obtain the initial values of (θ_i, ϕ_i) of the ith coil, i.e.

$$\theta_{i,0} = \pi/2 - \theta_s/2, \quad \phi_{i,0} = \pi(i-1)/6 \tag{21}$$

for coils $(i = 1, 2, \ldots, 12)$ at the upper layer, and

$$\theta_{i,0} = \pi/2 + \theta_s/2, \quad \phi_{i,0} = \pi(i-13)/6 \tag{22}$$

for coils $(i = 13, 14, \ldots, 24)$ at the lower layer. The subscript "0" represents the initial values of θ_i, ϕ_i.

Step 2: Calculation of the initial position of the coil axis. Take a unit vector starting from the rotor center along the axis of the ith coil. The Cartesian coordinates of the end point of

this vector in the rotor frame can be calculated as

$$\mathbf{p}_{i,0} = \begin{bmatrix} \sin\theta_{i,0}\cos\phi_{i,0} \\ \sin\theta_{i,0}\sin\phi_{i,0} \\ \cos\theta_{i,0} \end{bmatrix}. \tag{23}$$

Step 3: Compute the final position of the end point of the unit vector after rotor rotations. The final coordinates $\mathbf{p}_i$ of the point $\mathbf{p}_{i,0}$ in the rotor frame can be obtained via

$$\mathbf{p}_i = \begin{bmatrix} p_{ix} \\ p_{iy} \\ p_{iz} \end{bmatrix} = [\boldsymbol{R}_z(\phi_r)\boldsymbol{R}_y(\theta_r)\boldsymbol{R}_z(\delta_r)]^T \mathbf{p}_{i,0}$$

where p_{ix}, p_{iy}, and p_{iz} are components of $\mathbf{p}_i$.

Step 4: Computation of trigonometric functions of (θ_i, ϕ_i). To calculate the torque matrix $\boldsymbol{Q}$, values of θ_i, ϕ_i or their trigonometric functions can be calculated from the final coordinates of $\mathbf{p}_i$. A simple way to obtain $\boldsymbol{Q}$ is to calculate θ_i and ϕ_i, then substitute them into the torque matrix formula. This approach is easy to understand and can be employed to observe the torque variation corresponding to θ_i and ϕ_i. However, it takes long computation time due to the trigonometric functions in torque matrix, which may not be feasible for real-time motion control. An alternative approach is used to calculate the torque matrix $\boldsymbol{Q}$ by computing trigonometric functions of θ_i and ϕ_i from $\mathbf{p}_i$. $\boldsymbol{Q}$ is composed of $\sin\theta_i$, $\cos\theta_i$, $\sin\phi_i$, and $\cos\phi_i$ [15]. Solving functions of $\sin\theta_i$, $\cos\theta_i$, $\sin\phi_i$, and $\cos\phi_i$ from the final position $\mathbf{p}_i$ of the axis point directly could improve the computing efficiency considerably. Specifically, trigonometric functions of θ_i and ϕ_i are calculated as

$$\cos\phi_i = \frac{p_{ix}}{\sqrt{p_{ix}^2 + p_{iy}^2}}, \quad \sin\phi_i = \frac{p_{iy}}{\sqrt{p_{ix}^2 + p_{iy}^2}}$$
$$\cos\theta_i = p_{iz}, \quad \sin\theta_i = \sqrt{p_{ix}^2 + p_{iy}^2}. \tag{24}$$

Step 5: Complete solution of the torque matrix. Repeat the aforesaid computation for all coils. A complete set of trigonometric functions of θ_i and ϕ_i can be calculated. By using these values, the torque matrix $\boldsymbol{Q}$ can be obtained.

C. Computation of Condition Number

Torque matrix $\boldsymbol{Q}$ can be calculated corresponding to rotor orientations within the workspace, and thus the condition number. Repeat the computation of torque matrix by varying the angles ϕ_r, θ_r and δ_r within their ranges. Based on the result, the singularity property of the PM spherical actuator workspace can be evaluated.

The variation of the condition numbers can be visualized. By fixing ϕ_r at certain values such as $0°, 15°, 30°$, etc., a 3D plot of the condition number, denoted as n_c, with respect to the variation of θ_r and δ_r can be presented visually as a 2-D surface. By choosing different ϕ_r, a set of 2-D surfaces can be obtained, some of which are shown in Fig. 18. Due to the symmetric arrangement of the PM poles about the shaft, only the ranges of $\phi_r = 0°$–$45°$ and $\delta_r = 0°$–$45°$ are considered. Referring to Fig. 18, we can find that the condition numbers

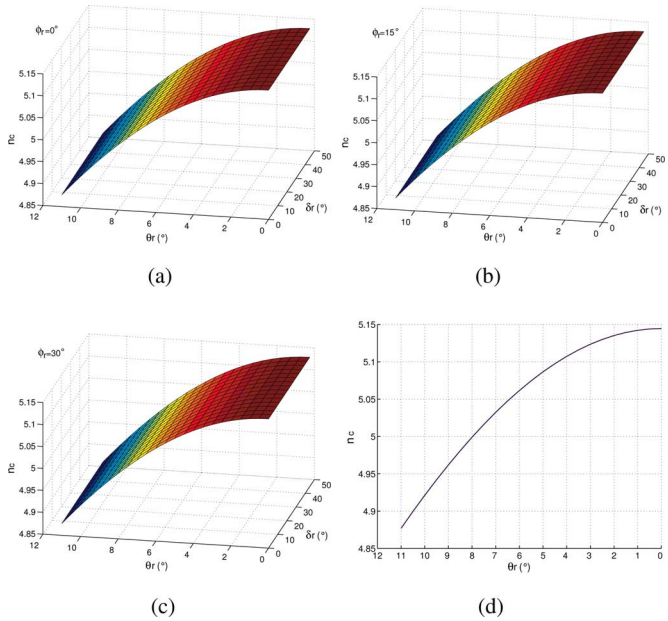

Fig. 18. Condition number of torque matrix $\boldsymbol{Q}$ (a) $\phi_r = 0°$. (b) $\phi_r = 15°$. (c) $\phi_r = 30°$. (d) Section view for $\phi_r = 30°$ and $\delta_r = 0$.

n_c do not vary too much with respect to δ_r and ϕ_r because of the evenly distributed PM poles along the rotor equator. It can also be found that the minimum value of the condition number is 4.877, whereas the maximum value is 5.145, which is of the same order of magnitude 1. Therefore the workspace of this PM spherical actuator is completely singularity-free.

VII. Conclusion

The torque model of a PM spherical actuator consisting of a rotor with eight PM poles along the equator and a stator with 24 coils symmetrically arranged with respect to the stator equator plane has been derived. The parametrization of PM and coil poles offers the opportunity for the actuator design to achieve maximum torque output. Based on the theoretical analysis, a research prototype has been developed that can be employed for future experimental investigation on magnetic field and torque variation. One significant feature of this actuator design is the singularity-free workspace, which is verified with condition numbers of torque matrix.

Acknowledgment

The authors would like to acknowledge the assistance from J. Su, Dr. W. Chen and T. S. M. Thomas.

References

[1] F. C. Williams, E. R. Laithwaite, and J. Eastham, "Development and design of spherical induction motors," *Proc. Inst. ELect. Eng.*, pp. 471–484, Dec. 1959.

[2] K. Davey, G. Vachtsevanos, and R. Powers, "The analysis of fields and torques in spherical induction motors," *IEEE Trans. Magn.*, vol. 23, no. 1, pp. 273–282, Jan. 1987.

[3] G. J. Vachtevanos, K. Davey, and K. M. Lee, "Development of a novel intelligent robotic manipulator," *IEEE Control Syst. Mag.*, vol. 7, no. 3, pp. 9–15, Jun. 1987.

[4] K. M. Lee, R. Roth, and Z. Zhou, "Dynamic modeling and control of a ball-joint-like variable-reluctance spherical motor," *ASME J. Dyn. Syst., Meas., Control*, vol. 118, no. 1, pp. 29–40, Mar. 1996.
[5] K. M. Lee, "Effects of fixture dynamics on back-stepping control of a VR spherical motor," in *Proc. 7th Int. Conf. Robot., Autom. Comput. Vision*, 2002, Singapore, pp. 1–6.
[6] Z. Zhou, "Real-time control and characterization of a variable reluctance spherical motor," Ph.D. dissertation, Georgia Inst. Technol. Atlanta, GA, May 1995.
[7] J. Wang, G. W. Jewell, and D. Howe, "Spherical actuators with multiple degrees-of-freedom," in *IEE Colloq. Limited Motion Electrical Actuation Systems*, vol. 494, pp. 8-1–8-6, Oct. 1998.
[8] J. Wang, G. W. Jewell, and D. Howe, "A novel spherical actuator with three degrees-of-freedom," in *IEEE Trans. Magn.*, vol. 34, no. 4, pp. 2078–2080, Jun. 1998.
[9] G. S. Chirikjian and D. Stein, "Kinematic design and commutation of a spherical stepper motor," *IEEE/ASME Trans. Mechatron.*, vol. 4, no. 4, pp. 342–353, Dec. 1999.
[10] C. Yang and Y. S. Baek, "Design and control of the 3 degrees of freedom actuator by controlling the electromagnetic force," *IEEE Trans. Magn.*, vol. 35, no. 5, pp. 3607–3609, Sep. 1999.
[11] K. Kahlen, I. Voss, C. Priebe, and R. W. De Doncker, "Torque control of a spherical machine with variable pole pitch," *IEEE Trans. Power Electron.*, vol. 19, no. 6, pp. 1628–1634, Nov. 2004.
[12] B. Dehez, G. Galary, and B. Raucent, "Development of a spherical induction motor with two degrees of freedom," *IEEE Trans. Magn.*, vol. 42, no. 8, pp. 2077–2088, Aug. 2006.
[13] L. Yan, I. M. Chen, C. K. Lim, G. L. Yang, W. Lin, and K. M. Lee, "Experimental investigation on the magnetic field of a permanent magnet spherical actuator," in *Proc. IEEE/ASME Int. Conf. Adv. Intell. Mechatron.*, California, Jul. 2005, pp. 347–352.
[14] L. Yan, I. M. Chen, G. L. Yang, and K. M. Lee, "Analytical and experimental investigation on the magnetic field and torque of a permanent magnet spherical actuator," *IEEE/ASME Trans. Mechatron.*, vol. 11, no. 4, pp. 409–419, Aug. 2006.
[15] L. Yan, I. M. Chen, C. K. Lim, G. L. Yang, W. Lin, and K. M. Lee, "Torque modeling of a spherical actuator based on lorentz force law," in *Proc. IEEE Int. Conf. Robot. Autom.*, Barcelona, Spain, Apr. 2005, pp. 3657–3662.
[16] Specification of transfer bearings. (2004). [Online]. Available: http://www.balltransfergroup.com.
[17] J. Wang, G. W. Jewell, and D. Howe, "Modelling of a novel spherical permanent magnet actuator," in *Proc. 1997 IEEE Int. Conf. Robot. Autom.*, Albuquerque, New Mexico, Apr. 1997, vol. 145, pp. 1190–1195.
[18] K. M. Lee, D. E. Ezenekwe, and T. He, "Design and control of a spherical air-bearing system for multi-d.o.f ball-joint-like actuators," *Mechatronics*, vol. 13, pp. 175–194, 2003.
[19] D. E. Ezenekwe, "Design methodology of an air bearing system for Multi-DOF spherical actuator motion control applications," Ph.D. dissertation, Georgia Inst. Technol. Atlanta, GA, Dec. 1998.
[20] Hephaist Seiko Co., Ltd. Specification of spherical bearings.
[21] J. J. Craig, *Introduction to Robotics: Mechanics and Control*. Reading, MA: Addison-Wesley, 1989.

Liang Yan (M'07) received the B. Eng. degree from North China Institute of Technology, Beijing, China, in 1995, the M. Eng. degree from Beijing Institute of Technology, Beijing, in 1998, and the Ph.D degree from Nanyang Technological University, Singapore, Singapore, in 2007, all in mechanical engineering.

From 1998 to 2002, he was a Lecturer at Beijing Institute of Technology. He is currently with Nanyang Technological University. His current research interests include electromagnetic actuators, sensors, navigation system, and expert system design.

Dr. Yan was the recipient of the National Defense Science and Technology Award, China in 2002. He is the Publication Chairman of the 2008 IEEE International Conference on Cybernetics and Intelligent Systems, the 2008 IEEE International Conference on Robotics, Automation and Mechatronics.

I-Ming Chen (M'95–SM'06) received the B.S. degree from the National Taiwan University, Taipei, Taiwan, R.O.C, in 1986, and the M.S. and Ph.D. degrees from California Institute of Technology, Pasadena, in 1989 and 1994, respectively, all in mechanical engineering.

During 1999, he was a Visiting Scholar at the Japan Society for the Promotion of Science (JSPS), Kyoto University, Kyoto, Japan. During 2004, he was with Massachusetts Institute of Technolgy (MIT), Cambridge, in 2004. Since 1995, he has been with the School of Mechanical and Aerospace Engineering, Nanyang Technological University, Singapore. He is currently a Fellow of Singapore-MIT Alliance under Manufacturing Systems and Technology (MST) Program. He is also an Adjunct Professor at Xian Jiao Tong University, China. His current research interests include in reconfigurable automation, biomedical applications of reconfigurable robotic systems, parallel kinematics machines (PKM), biomorphic underwater robots, and smart material based actuators. He is the author or coauthor of more than 130 technical articles published in refereed international journals and conferences. He is currently a member of the Editorial Board for the Robotica-International Journal.

Dr. Chen is currently a member of the Editorial Board for the IEEE/ American Society of Mechanical Engineers (ASME) TRANSACTIONS ON MECHATRONICS and Steering Committee of the International Federation for the Promotion of Mechanism and Machine Science (CISM)-(IFToMM) Symposium on Robot Design, Dynamics and Control (ROMANSY). He is also General Chairman of 2009 IEEE/ASME International Conference on Advanced Intelligent Mechatronics (AIM2009), Singapore. He is member of ASME and the RoboCup Singapore National Committee.

Chee Kian Lim received the B. Eng., M. Eng., and Ph.D. degrees in mechanical engineering from Nanyang Technological University (NTU), Singapore, Singapore, in 1998 and 2000, respectively.

During 2000–2002, he was an Assembly Product Engineer at Micron Semiconductor Asia. He is currently a Research Associate at NTU. His current research interests include smart actuators with special empasis on electromagnetic and ultrasonic motors, electromagnetic actuators, sensors, navigation system, and expert system design.

Guilin Yang (M'02) received the B. Eng. and M. Eng. degrees from Jilin University, Changchun, China, in 1985 and 1988, respectively, and the Ph.D. degree from Nanyang Technological University, Singapore, in 1999, all in mechanical engineering.

During 1988, he was with the School of Mechanical Engineering, Shijiazhuang Railway Institute, China, earlier as a Lecturer, a Division Head, and then, the Vice-Dean. He is currently a Research Scientist and the Deputy Group Manager of the Mechanics Group, Singapore Institute of Manufacturing Technology, Singapore, Singapore. His current research interests include computational kinematics, multibody dynamics, parallel-kinematics machines, modular robots, flexure-based precision mechanisms, electromagnetic actuators, rehabilitation devices, and industrial robot systems. He is the author or coauthor of more than 100 technical papers published in refereed international journals and conferences.

Dr. Yang is a Technical Committee Member for the Robotics of International Federation for the Promotion of Mechanism and Machine Science (IFToMM) and the Secretary of Singapore Chapter of IEEE Robotics and Automation Society.

Wei Lin (M'03) recieved the B.Sc. degree from the University College, London, U.K. in 1985, and the M.Sc. and Ph.D. degrees from the University of Florida, Gainesville, in 1988 and 1992, respectively, all in mechanical engineering.

Since 1992, he has been with Singapore Institute of Manufacturing Technology, Singapore, Singapore, where he is currently a Senior Scientist and the Manager of the Mechatronics Group. He is also an Adjunct Associate Professor at the National University of Singapore, Singapore, and Nanyang Technological University, Singapore. His current research interests include high-precision positioning system, micromanipulation for flexible material, and microsystem assembly.

Kok-Meng Lee (M'89–SM'02–F'05) received the B.S. degree from the State University of New York, Buffalo, in 1980, and the S.M. and Ph.D. degrees from the Massachusetts Institute of Technology, Cambridge, in 1982 and 1985, respectively.

He is a currently a Professor at the Woodruff School of Mechanical Engineering, Georgia Institute of Technology, Atlanta. His current research interests include system dynamics/control, robotics, automation, and mechatronics. He holds eight patents in machine vision, three in degrees of freedom (DOF) spherical motor/encoder and live-bird handling system.

Dr. Lee is a Fellow of the American Society of Mechanical Engineers (ASME). He was the recipient of the National Science Foundation (NSF) Presidential Young Investigator, Sigma Xi Junior Faculty Research, International Hall of Fame New Technology, and Kayamori Best Paper Awards.